

An improved combination of Hilbert and Park transforms for fault detection and identification in three-phase induction motors

Khmais Bacha ^{*}, Samira Ben Salem, Abdelkader Chaari

Unit of Research Control, Monitoring and Reliability of The Systems, Higher School of Sciences and Technology of Tunis, 5, Taha Hussein Street, Tunis, Post Box 56, Bab Menara 1008, Tunisia

ARTICLE INFO

Article history:

Received 6 December 2011

Received in revised form 10 April 2012

Accepted 9 June 2012

Available online 15 July 2012

Keywords:

Fault diagnosis

Hilbert transform

Park transform

Support vector machine

ABSTRACT

In this work we propose an original fault signature based on an improved combination of Hilbert and Park transforms. Starting from this combination we can release two fault signatures: Hilbert modulus current space vector (HMCSV) and Hilbert phase current space vector (HPCSV). These two signatures are subsequently analyzed using the classical fast Fourier transform (FFT). The effects of HMSCV and HPCSV spectrums are described and the related frequencies are determined. A comparative study is presented of the suggested signature (HPCSV) and the MCSA which is the signature more recently proposed in the literature. The proposed signature shows its effectiveness and its robustness in both electrical and mechanical fault detection. The magnitudes of spectral components relative to the studied faults are extracted in order to develop the input vector necessary for the pattern recognition tool based on support vector machine (SVM) approach with an aim of classifying automatically the various states of the induction motor. This approach was applied to a 1.1 kw induction motor under normal operation and with the following faults: unbalanced voltage, broken rotor bar, air-gap eccentricity and outer raceway ball bearing defect.

© 2012 Elsevier Ltd. All rights reserved.

1. Introduction

Induction motors are nowadays extensively used in all types of industry applications due to their simple construction, reliability, and the availability of power converters using efficient control strategies. In this way, early fault detection and diagnosis allow preventative and condition-based maintenance to be arranged for the electrical machines during scheduled downtimes and prevent an extended period of breakdown due to extensive system failures. For the fault detection problem, it is interesting to know if a fault exists in the system via online measurements. For the fault diagnosis one, it is not only worthwhile to detect if the system has a fault but also to insulate the fault and to find its origin [1].

Although induction machines are failures subjected which are inherent to the machine itself or due to external environment. The origins of inherent failures are due to the mechanical or electrical forces acting in the machine enclosure. Researchers have studied a variety of machine faults, such as winding faults [2], voltage unbalance [3,4], broken rotor bars [5], eccentricity [6], and bearing faults [7].

Various methods for induction motor fault detection have been reported in the literature. In [8], an online induction motor diagno-

sis system using motor current signature analysis (MCSA) with advanced signal processing algorithms is proposed. In [9], authors propose a method based on monitoring certain statistical parameters estimated from the analysis of the steady state stator current. The approach is based on the extraction of the signal envelop by Hilbert transformation, pre-multiplied by a Tukey window to avoid transient distortion. In [10], authors use a sliding window constructed by Hilbert transform of one current phase and the fault severity is diagnosed by motor current signature analysis (MCSA) of the stored Hilbert transform of several periods.

Besides the traditional current signature analysis based on one-phase current spectrum lines, the procedures based on the analysis of the harmonics at fault frequency in the spectrum respectively of instantaneous power, space vector current modulus and electromagnetic torque are presented in [11]. In [12], a method based on Park's vector approach for bearing fault detection using three-phase stator current analysis is presented. In [13], author describes the use of the Extended Park's Vector Approach (EPVA) for diagnosing the occurrence of stator winding faults in operating three-phase induction motor. In [14], the authors take the initial step to investigate the efficiency stray flux monitoring for induction motor fault diagnosis. The effects of stray flux spectrum are described and the related frequencies are determined.

Several researchers have used the artificial intelligence tools in order to classify faults in electrical power systems. In [15], authors

* Corresponding author. Tel.: +216 98 500 501.

E-mail addresses: khmais-bacha@voila.fr (K. Bacha), samira-bensalem@voila.fr (S.B. Salem), abdelkader.chaari@yahoo.fr (A. Chaari).

propose an approach to obtain objective function using the Hebb's learning rule. The continuous genetic algorithm optimization method is used to estimate the fault section making use of the objective function. A comparison with artificial neural network approach is also presented. In [16], the pattern classification technology and linear discrimination principle of pattern recognition theory are used in order to identify the fault components and fault sections, and eventually accomplish fault isolation.

In this work we propose an original fault signature based on an improved combination of Hilbert and Park transforms. Starting from this combination we can release two fault signatures: Hilbert modulus current space vector (HMCSV) and Hilbert phase current space vector (HPCSV). These two signatures are subsequently analyzed using the classical fast Fourier transform (FFT). A comparative study is presented of the suggested signature (HPCSV) and the MCSA which is the signature more recently proposed in the literature. The magnitudes of the HPCSV spectral components relative to the studied faults are extracted in order to develop the input vector necessary for the pattern recognition tool based on support vector machine (SVM) approach with an aim of classifying automatically the various states of the induction motor.

This approach was applied to a 1.1 kw induction motor under normal operation and with the following faults: unbalanced voltage, broken rotor bar, air-gap eccentricity and outer raceway bearing defect.

2. Basic theory of the proposed fault signature

The basic idea is instead of using directly the three lines currents to calculate the park vector, we only employ useful information immersed in these currents. For this reason we apply the Hilbert transform to the three line currents. Indeed Hilbert transform is used to acquire the instantaneous frequency and instantaneous amplitude. It reveals modulation in signals caused by faulty components. In addition, it removes carrier signals and this will reduce the influence of irrelevant information for the purpose of fault detection.

Fig. 1 illustrates the block diagram of the proposed induction motor fault signatures. The development of our fault signatures requires initially the calculation of the modulus and the phase of the Hilbert transform of each three lines current. Thereafter we apply the Park transform to the three phases and three modules. After the Park transformation we calculate the space vector relating to the modulus and at the phase. In the continuation, we will present the principal concepts of the Hilbert and the Park transforms.

2.1. Demodulations by Hilbert transform

The demodulation consists in extracting from the signal, the functions of phase and amplitude modulation.

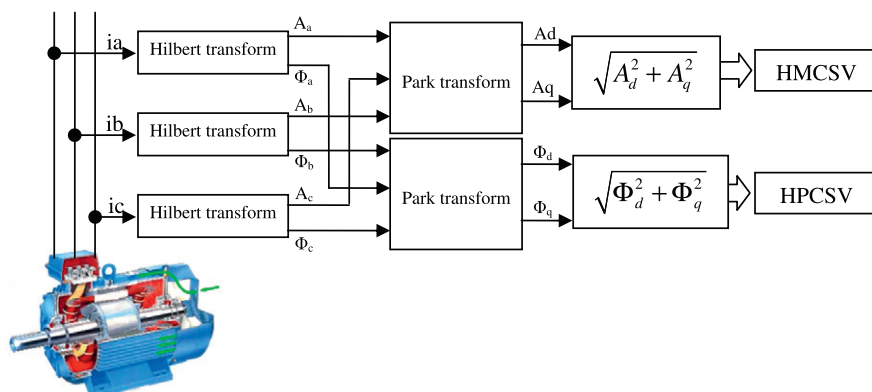


Fig. 1. The proposed fault signatures for induction motor monitoring.

The frequency and amplitude modulation can be expressed as:

$$x(t) = A(t) \sin \psi(t) \quad (1)$$

where $A(t)$ expresses the amplitude modulation and $\psi(t)$ expresses the instantaneous phase.

The instantaneous phase $\psi(t)$ is expressed as:

$$\psi(t) = \omega t + \Phi(t) \quad (2)$$

where $\Phi(t)$ expresses the phase modulation.

The instantaneous pulsation of the signal ω_{inst} is equal to derived from the instantaneous phase:

$$\omega_{inst} = \frac{d}{dt}(\psi(t)) = \omega + \frac{d}{dt}(\Phi(t)) \quad (3)$$

The equation $x(t)$ of a modulated signal is expressed as:

$$x(t) = A(t) \sin(\omega t + \Phi(t)) \quad (4)$$

We can form an analytical signal while adding to the modulated signal $x(t)$, the Hilbert transform $H(x(t))$ in his imaginary part:

$$\tilde{x}(t) = x(t) + iH(x(t)) \quad (5)$$

The Hilbert transform is expressed as:

$$H(x(t)) = \frac{1}{\pi} \int_{-\infty}^{+\infty} x(\tau) \frac{1}{1 - \tau} d\tau \quad (6)$$

In other way, the Hilbert transform corresponds to the convolution of $x(t)$ by $1/\pi\tau$:

$$H(x(t)) = x(t) * 1/\pi\tau \quad (7)$$

where $*$ is the convolution indicate.

The function of amplitude modulation $A(t)$ (amplitude of the envelop) is expressed as:

$$A(t) = \sqrt{x^2(t) + H^2(x(t))} \quad (8)$$

The function of phase modulation $\Phi(t)$ (instantaneous phase) is expressed as:

$$\Phi(t) = \tan^{-1} \left(\frac{H(x(t))}{x(t)} \right) \quad (9)$$

The instantaneous pulsation $\omega(t)$ becomes (in rad/s):

$$\omega(t) = \omega + \frac{d}{dt}(\Phi(t)) \quad (10)$$

The Hilbert function of the $H(x(t))$ signal thus makes it possible to calculate the functions of phase and amplitude modulation as well as the instantaneous frequency by using the equations of $A(t)$, $\Phi(t)$ and $\omega(t)$.

The demodulation is a very powerful tool to detect any defect which causes the modulation of the signal.

2.2. The Park transform

The Park transform consists in passing from a three-phase system to a two-phase system.

A two-dimensional representation can then be used for describing three-phase induction motor phenomena; a suitable one is being based on the Park's vector.

As a function of mains phase variables ($x_a; x_b; x_c$) the Park's vector components ($x_d; x_q$) are:

$$x_d(t) = \sqrt{\frac{2}{3}}x_a(t) - \frac{1}{\sqrt{6}}x_b(t) - \frac{1}{\sqrt{6}}x_c(t) \quad (11)$$

$$x_q(t) = \frac{1}{\sqrt{2}}x_b(t) - \frac{1}{\sqrt{2}}x_c(t) \quad (12)$$

The space vector is calculated by the following relationship:

$$x_s(t) = \sqrt{x_d^2(t) + x_q^2(t)} \quad (13)$$

3. Basic theory of the SVM

The basic concept of the SVM is detailed in [17]. SVM analysis seeks to find an optimal separating hyper-plane by maximizing the margin between the separating data.

The regression approximation estimates a function according to a given data set $T = \{x_k, y_k\}_k^m$, where x_k denotes the input vector, $y_k \in \{-1; 1\}$ denotes the corresponding output value and m denotes the total number of data patterns, the SVM regression function is:

$$f(x) = w \cdot x + b = \sum_{k=1}^m w_k \cdot x_k + b = 0 \quad (14)$$

where w denotes the weight vector and b denotes the bias term. w and b are used to define the position of the separating hyper-plane by which should satisfy the constraints:

$$\begin{cases} y_k(w \cdot x_k + b) \geq 1, & k = 1, 2, \dots, m \\ \min \frac{1}{2} \|w\|^2 \end{cases} \quad (15)$$

According to Lagrangian principle, the above problem can be transformed to its corresponding form as follows:

$$L(w, b, \alpha) = \frac{1}{2} w^T w - \sum_{k=1}^m \alpha_k [y_k(w^T x_k + b) - 1] \quad (16)$$

where α_k are the Lagrange coefficients ($\alpha_k > 0$).

According to the condition of optimality:

$$\frac{\partial L(w, b, \alpha)}{\partial w} = 0, \quad \frac{\partial L(w, b, \alpha)}{\partial b} = 0 \quad (17)$$

We have the following equations:

$$\begin{cases} w = \sum_{k=1}^m \alpha_k x_k \cdot y_k \\ \sum_{k=1}^m \alpha_k y_k = 0 \end{cases} \quad (18)$$

Hence, from Eqs. (16) and (18), the dual problem is:

$$\begin{cases} \max \sum_{k=1}^m \alpha_k - \frac{1}{2} \sum_{k,j} \alpha_k \alpha_j y_k y_j (x_k \cdot x_j) \\ \forall k, \quad \alpha_k \geq 0 \\ \sum_{k=1}^m \alpha_k y_k = 0 \end{cases} \quad (19)$$

We define the support vectors VS any vector x_k as:

$$y_k \cdot [(w_0 \cdot x_k) + b_0] = 1 \quad (20)$$

This is equivalent to Eq. (21):

$$VS = \{x_k | \alpha_k > 0\} \quad \text{for } k = 1, 2, \dots, m \quad (21)$$

The ranking function class (x) is defined by Eq. (22):

$$class(x) = sign[(w_0 \cdot x) + b_0] = sign \left[\sum_{i \in VS}^n \alpha_i y_i (x_i \cdot x) + b_0 \right] \quad (22)$$

If class (x) is less than 0, x is the class –1 else it is a class 1.

However, for nonlinear cases, there is insufficient space for classifying the inputs. So, we need a larger space. We must therefore resolve the following equation:

$$\begin{cases} \max \sum_{k=1}^m \alpha_k - \frac{1}{2} \sum_{k,j} \alpha_k \alpha_j y_k y_j \phi(x_k) \phi(x_j) \\ \forall k, \quad 0 \leq \alpha_k \leq C \\ \sum_{k=1}^m \alpha_k y_k = 0 \end{cases} \quad (23)$$

With C is the margin parameter.

$K(x_k, x_j) = \phi(x_k) \cdot \phi(x_j)$ is a positive kernel function definite on R^n based on Mercy condition.

From the above analysis, it can be concluded that SVM is decided by training samples and kernel function. The construction and selection of kernel function is important to SVM. But the kernel function is often given directly in practice.

Some common kernel functions are shown as follows:

- The linear kernel function:

$$K(x, x') = x \cdot x' \quad (24)$$

- The polynomial kernel function:

$$K(x, x') = (x \cdot x')^d \text{ or } (c + x \cdot x')^d \quad (25)$$

- Gaussian radial basis function:

$$K(x, x') = \exp \left(-\frac{\|x - x'\|^2}{2\sigma^2} \right) \quad (26)$$

- Sigmoid kernel function:

$$K(x, x') = \tanh(\alpha_0(x, x') + \beta_0) \quad (27)$$

4. Experimental results

4.1. Test bench description

The test motor used in the experimental investigation was a three-phase 50-Hz, four-pole, 28 rotor bars, 1.1-kW induction machine (Fig. 2a). The induction machine shaft is mounted with a powder brake in order to simulate different level of load torque during the tests.

The studied faults are: broken rotor bar, unbalanced voltage, one air-gap eccentricity and the outer raceway ball bearing defect.

The machine with broken rotor bar is faulted by drilling a hole on all its depth. Stator voltages were unbalanced by adding a resistance to one phase. In order to create an air-gap eccentricity fault in the induction motor, a simple mechanism was used. Each of the two bearing housings of the rotor was changed to a pair of eccentric rings placed one into the other (Fig. 2b). The defective bearings were installed on the load side of the induction motor. The diagnosis of bearing failures on the load side of the mechanics succeeds as well. The generated artificial faults that have been installed for the following results are shown in Fig. 2c for the outer raceway faults. Eroding the rings of the bearings resulted in a slot with a width of 5 mm at the outer raceway. The investigated bearings contain nine balls.

Three phase current sensors are used to monitor the induction machine during operation at steady state. Low-pass anti-aliasing filters are implemented in order to set the frequency bandwidth of the analyzed signals to a correct range. Then, the outputs of

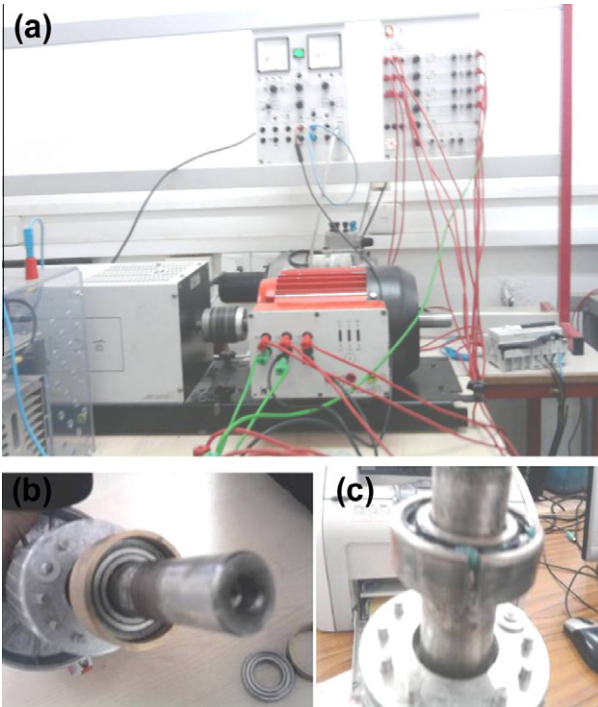


Fig. 2. Experimental set-up of 1.1 kW to collect healthy and faulty induction machine data. in stator current.

the low-pass filters are directly connected to a data acquisition board (dSpace DS1104 processor board) which contains a Motorola Power PC 603e model and a DSP (TMS320F240 – 20 MHz). The process can be commanded and monitored via the Control Desk software of dSpace. The data sampling is performed using differential channels and a sampling frequency of 10 kHz. The software used is MATLAB™ for the data acquisition and processing.

In order to test the efficiency of the proposed diagnostics techniques, the proposed fault signatures are analyzed in the frequency domain. The Blackman window is chosen because it gives the best compromise between the relative side lobe attenuation and the main lobe width, in order to differentiate the analyzed frequency components used by the tested diagnosis methods. The choice of the Blackman window is detailed in [18].

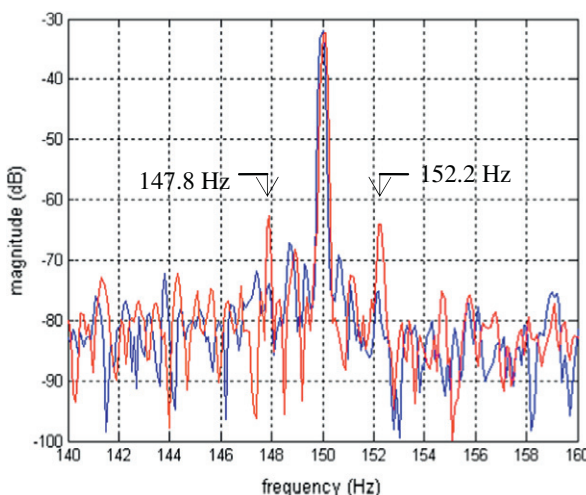


Fig. 3. HMCSV spectrum at full load in the case of: normal condition (blue) and broken rotor bar (red).

Table 1

Sensitivity of frequency components related to the broken rotor bar fault ($k = 1$).

m	3	6	9	
f_{bb} (Hz)	147.8	152.2	297.8	302.2
HMSCV (dB)	11.2	10.6	10	20
HPCSV (dB)	19.4	18.2	20	17.5
			22.5	16.3

4.2. Hilbert current space vector analysis in the case of broken rotor bar

The existence of a rotor cage fault will result in electrical asymmetry of the rotor circuit. This will give rise to the $(1 - 2s)f$, harmonic components in the stator current and their magnitudes reflect the severity of the rotor asymmetry as shown by numerous authors. the interaction of the $(1 - 2s)f$ harmonic component of the stator current with the fundamental air-gap flux produces a speed ripple at $2sf$ and gives rise to additional stator current harmonics at frequencies $(1 \pm 2ks)f$ with f : fundamental frequency (50 Hz), s : slip, $k = 1, 2, 3$.

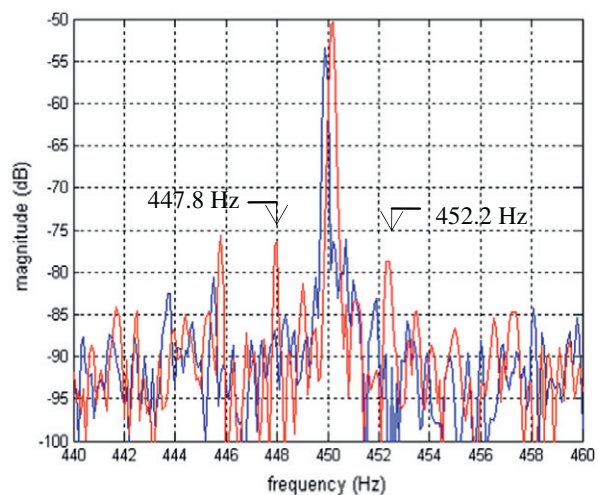
On the other hand, all the tests have been performed at rated load ($s = 0.022$) in order to compared the real accuracies of all the proposed techniques. This is only possible at constant speed since the harmonic magnitudes are sensible to rotor speed taking into account that the observation of side-band harmonics needs relative accuracy better than 0.1%.

In fact, any rotor asymmetry introduces two lines in the Hilbert current space vector spectrum separated of $\pm 2sf$ from the multiples of the supply frequency.

$$f_{bb} = (1 \pm 2ks)mf \quad (28)$$

with $k = 1, 2, 3$ and $m = 1, 2, 3\dots$

The rotor bar breakage can be observed in the Hilbert modulus current space vector (HMSCV) (Fig. 3) and the Hilbert phase current space vector (HPCSV) spectra (Fig. 4) at several frequency ranges. The fault sensitivity of each diagnosis media can be obtained comparing the magnitudes of the frequency components with respect to their initial value in healthy conditions. This sensitivity is reported in Table 1 and the analysis shows, that for the three broken bars, the related frequencies are more excited in the HPCSV (sensitivity around 20 dB) than in the HMSCV (sensitivity around 10 dB). The most significant frequencies are the frequencies calculated for m a multiple of 3 and $k = 1$.



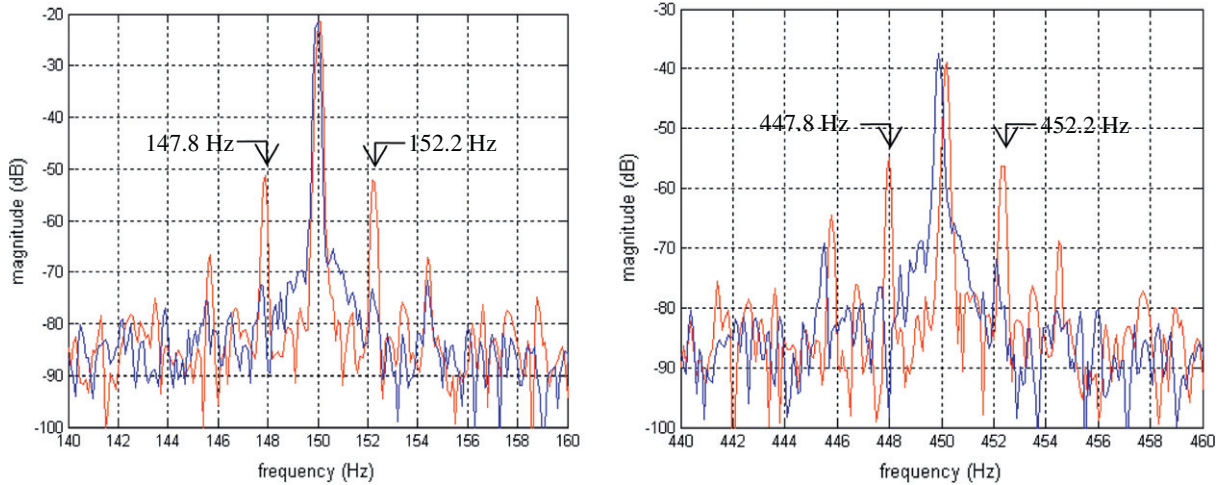


Fig. 4. HPCSV spectrum at full load in the case of: normal condition (blue) and broken rotor bar (red).

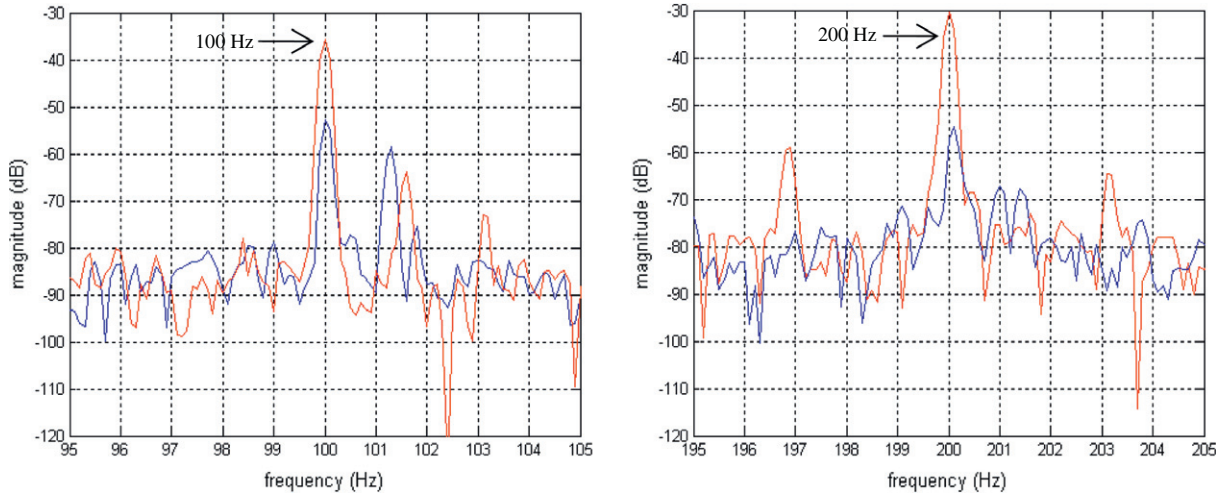


Fig. 5. HMCSV spectrum at full load in the case of: normal condition (blue) and under voltage unbalance (red).

4.3. Hilbert current space vector analysis in the case of the voltage asymmetry

The influence of the voltage asymmetry is evaluated applying on one phase –15% of voltage imbalance. In the HMCSV spectrum (Fig. 5) and the HPCSV spectrum (Fig. 6), it is shown that the 100 Hz and 200 Hz frequency components are affected by the voltage asymmetry. The important relative value of the double grid frequency shows clearly the voltage asymmetry influence on the HMCSV and MPCSV spectrum. The sensitivity for each diagnostic media is evaluated in Table 2. The obtained results show that the double grid frequency sensitivity is approximately the same for both techniques and it is around 20 dB.

4.4. Hilbert current space vector analysis in the case of the air-gap eccentricity fault

In reality, static and dynamic eccentricities tend to coexist. Ideal centric conditions can never be assumed. Therefore, an inherent grade of eccentricity is implied for any real machine, even in newly manufactured ones due to the manufacturing and assembly methods. When static and dynamic eccentricities are present, low fre-

quency components also appear in the current spectrum, which can be given by: $|f \pm mf_r|$.

where f_r is the rotor rotation frequency in rps and m is an arbitrary integer number. In fact, any air-gap eccentricity fault introduces two lines in the Hilbert current space vector spectrum separated of $\pm mfr$ from the supply frequency multiple.

$$f_{ecc} = |kf \pm mf_r| \quad (29)$$

with $k = 1, 2, 3$ and $m = 1, 3, 5, \dots$

The frequencies related at the air-gap eccentricity fault are summarized in Table 3. To show the efficiency of the proposed method, some selected spectra are presented. It can be seen that the spectral components coincide with the predicted values (Figs. 7 and 8).

Table 2
Sensitivity of frequency components related to the unbalanced voltage.

f (Hz)	100	200
HMSCV (dB)	16.9	24.6
HPCSV (dB)	18.4	21.5

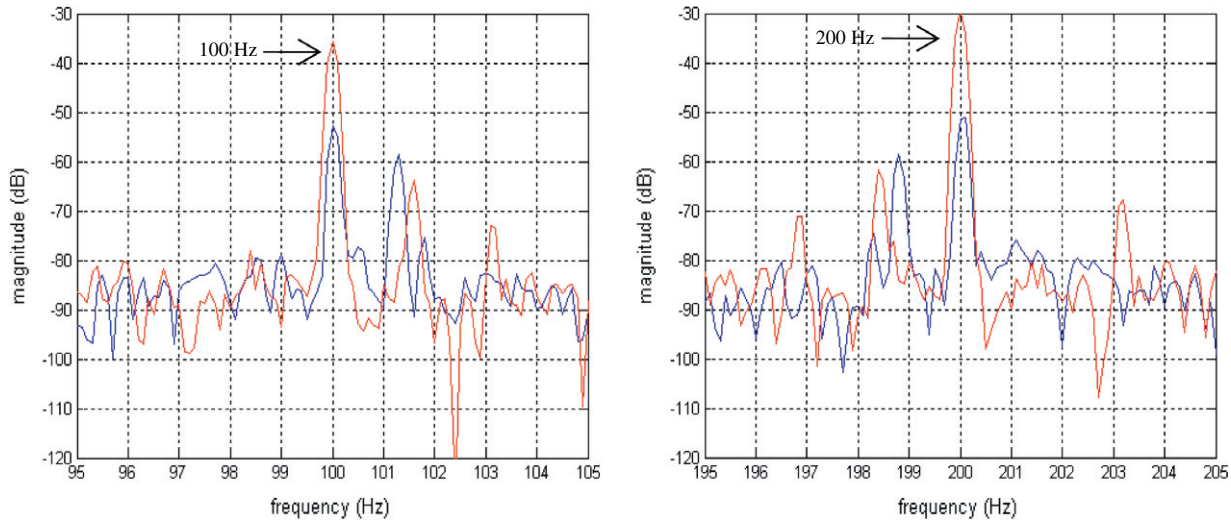


Fig. 6. HPCSV spectrum at full load in the case of: normal condition (blue) and under voltage unbalance (red).

Table 3
Different frequency component (in hertz) related to the air-gap eccentricity fault.

m	k					
		1	2	3	4	5
1	25.9	74.1	75.9	124.1	174.1	125.9
3	22.3	122.3	27.7	172.3	77.7	222.3

For $m = 1$ and $k = 3$, there are two harmonic components around 150 Hz (125.9 Hz and 174.1 Hz) in HMCSV (Fig. 7) and HPCSV (Fig. 8) spectrums. For $m = 3$ and $k = 1, 2$, there are four harmonic components (22.3 Hz, 27.7 Hz, 122.3 Hz and 172.3 Hz) in HPCSV spectrum (Fig. 8), normally these four components are used as index. The related frequencies are more excited in the HPCSV (sensitivity around 15 dB) than in the HMCSV (sensitivity around 10 dB). The HPCSV is richer in harmonics than the HMCSV spectrum. Only the HPCSV present more other frequency components (Table 3) related at the air-gap eccentricity fault around 50 Hz, 150 Hz... and 1350 Hz (Fig. 8) with a sensitivity around 15 dB.

4.5. Hilbert current space vector analysis in the case of the outer raceway bearing fault

The outer raceway ball bearing defect causes the appearance of characteristic fault frequencies in the spectrum of the measured parameters which are often utilized for fault diagnosis. The characteristic fault frequencies depend on the mechanical dimensions of the bearing, the number z of bearing balls, and the rotational frequency f_r of the inner raceway for a fixed outer ring. For bearings with between 6 and 12 balls, the fault frequencies for an outer raceway defect can be approximated using the following: $0.4zf_r$.

For outer raceway ball bearing fault, the following harmonics exists in the Hilbert current space vector spectrum:

$$f_{or} = |kf \pm 2f_d| \quad (30)$$

With $f_d = 0.4z f_r = 86.76$ Hz ($z = 9$ balls and $f_r = 24.1$ Hz) The outer raceway ball bearing fault can be observed in the HMCSV spectrum only in $(kf + 2f_d)$ (Fig. 9) and the HPCSV spectrum at several frequency ranges ($|kf \pm 2f_d|$) (Fig. 10). These frequencies are summarized in Table 4. The fault sensitivity of each diagnosis media can be obtained comparing the magnitudes of the frequency components with respect to their initial value in healthy conditions. The

obtained results show that the fault frequency sensitivity in $(kf + 2f_d)$ is approximately the same for both techniques and it is around 25 dB. But the HPCSV spectrum is richer in harmonics than the HMCSV, in fact the HPCSV spectrum contains in more harmonics ($|kf - 2f_d|$).

4.6. Comparative study of the performance of HPCSV, and the MCSA

In the following, we present a comparative study between the suggested signature (HPCSV) and the MCSA which is the signature more recently proposed in the literature. In this context we compare the sensitivity for different types of defects.

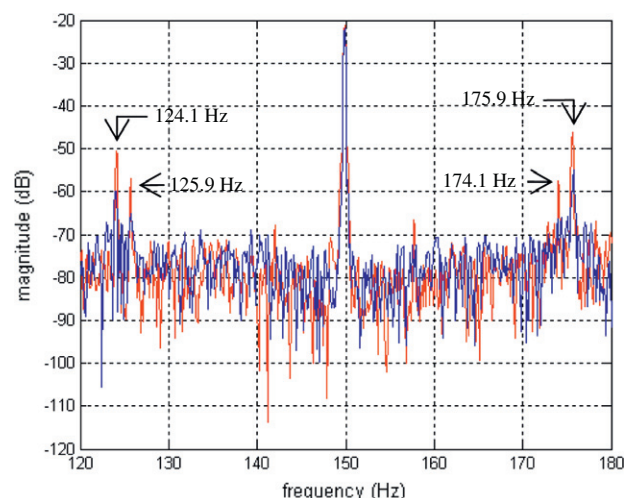


Fig. 7. HMCSV spectrum in the case of: normal condition (blue) and eccentricity fault (red).

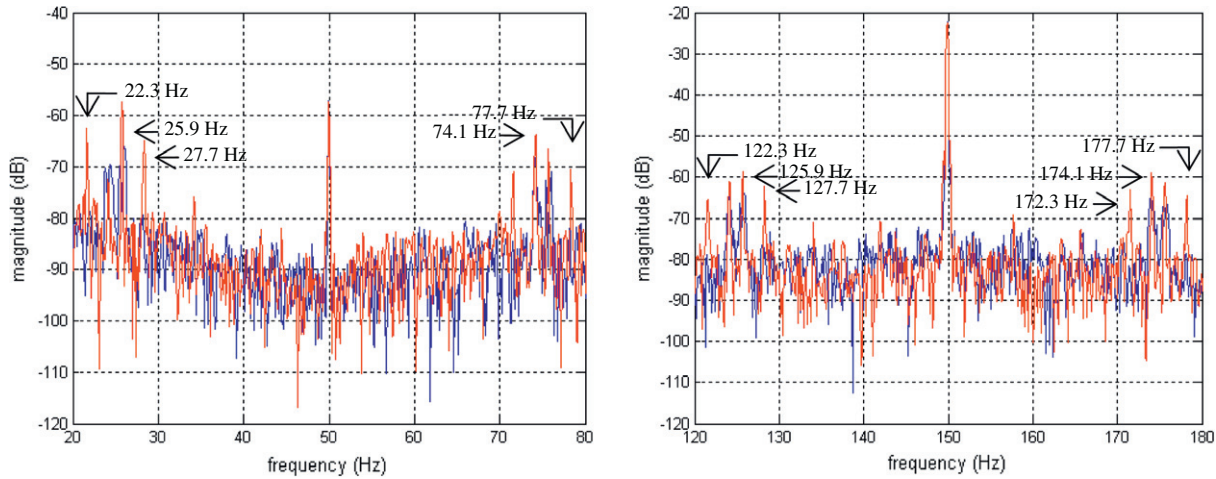


Fig. 8. HPCSV spectrum at full load in the case of: normal condition (blue) and air-gap eccentricity fault (red).

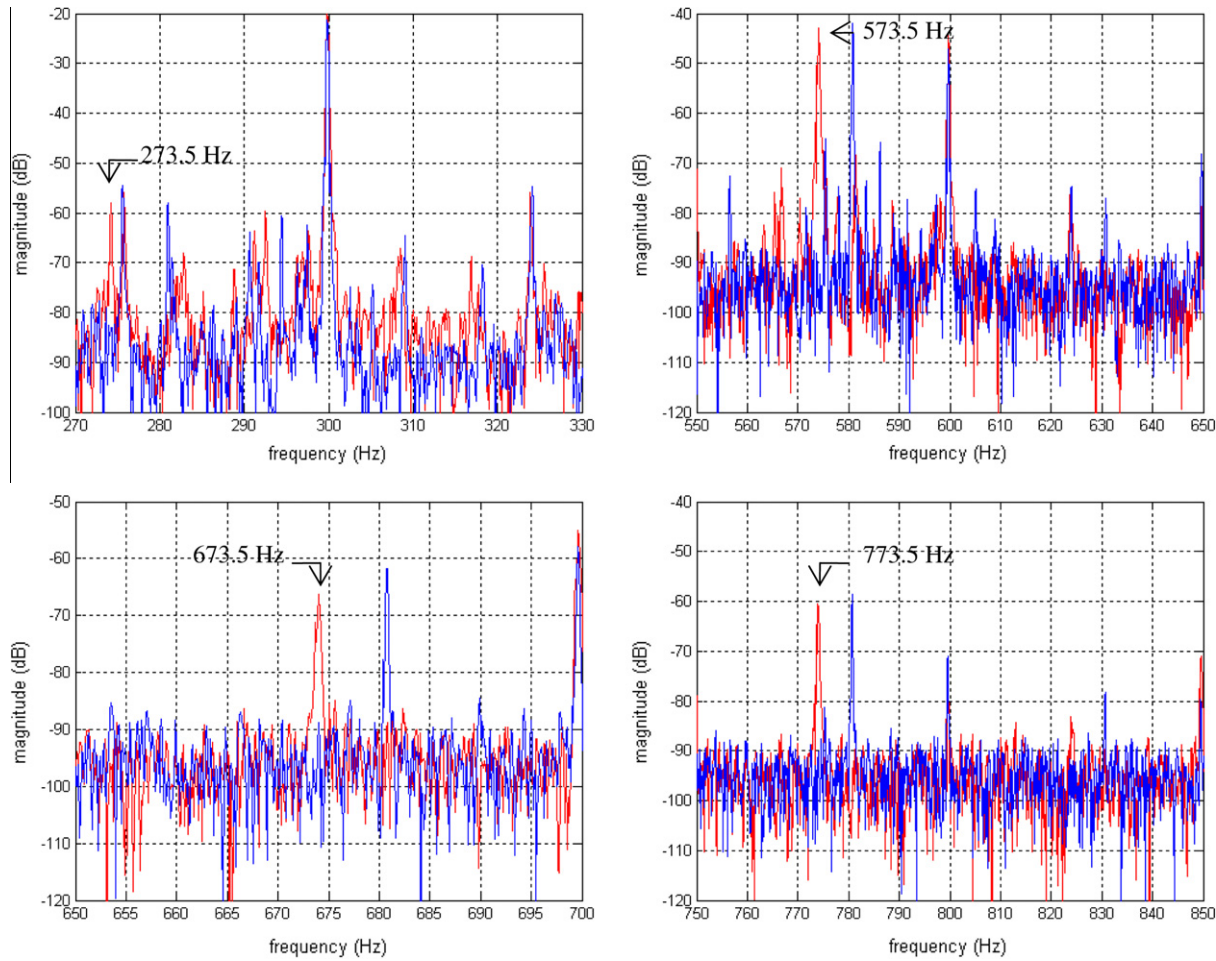


Fig. 9. HMCSV spectrum at full load in the case of: normal condition (blue) and outer raceway ball bearing fault (red).

In the case of the rotor broken bars, the MCSA shows a characteristic component at 47.8 Hz, and 52.2 Hz, which corresponds respectively to the frequency combination $(1 - 2s)f$ and $(1 + 2s)f$ (see Fig. 11). Amplitude in the faulty case (red¹ line) is obviously

increased compared to the healthy case (blue line), the sensitivity is around 20 dB.

However, for high frequency, the proposed signature has sensitivity better than the MCSA; we can see this in Fig. 12 where we present the MCSA around 250 Hz and 350 Hz in the case of the broken rotor bars.

The MCSA is used in order to detect the air-gap eccentricity fault. In Fig. 13, the MCSA shows a characteristic component at

¹ For interpretation of color in Figs. 1–15, the reader is referred to the web version of this article.

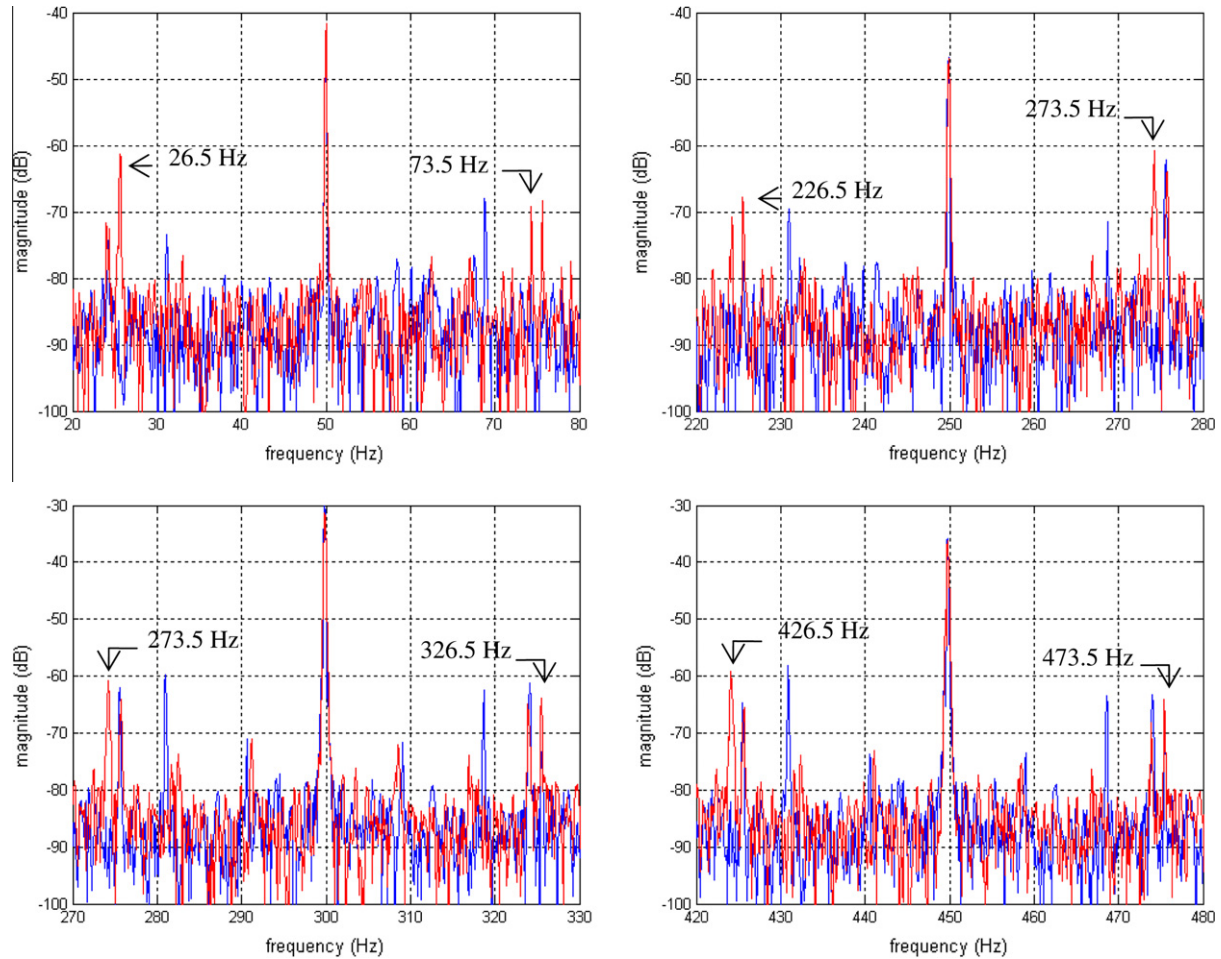


Fig. 10. HPCSV spectrum at full load in the case of: normal condition (blue) and outer raceway ball bearing fault (red).

25.9 Hz and 74.1 Hz, which corresponds respectively to the frequency combination $f - f_r$ and $f + f_r$. Amplitude in the faulty case (red line) is obviously increased compared to the healthy case (blue line), the sensitivity is respectively around 10 dB. Comparing the sensitivity, the HPCSV is better than the MCSA. Moreover, the spectrum of the suggested fault signature is richer in fault characteristic harmonics than the MCSA.

Concerning the outer raceway bearing fault, the MCSA shows a characteristic component at 33 Hz, which corresponds to the frequency combination $|f - f_d|$ (see Fig. 14). Amplitude in the faulty case (red line) is obviously increased in 33 Hz compared to the healthy case (blue line), the sensitivity is around 10 dB. Comparing the sensitivity, our fault signature is better than the MCSA. Moreover, the spectrum of the suggested fault signature is richer in fault characteristic harmonics than the MCSA.

We have chosen the HPCSV as fault signature because it offers the best sensitivity to the faults and it presents harmonics on a large frequency band.

4.7. Induction motor faults classification based on SVM

Fig. 15 shows that the HPCSV spectrum is very rich in harmonics; they are spread out up to 2000 Hz, whereas the harmonics of the HMSCV spectrum are limited to 1200 Hz.

We chose the HPCSV as fault signature because it offers the best sensitivity to the faults and it presents harmonics on a large frequency band.

The magnitudes of HPCSV spectral components relative to the studied faults are extracted in order to develop the input vector necessary for the pattern recognition tool based on support vector machine (SVM) approach with an aim of classifying automatically the various states of the induction motor.

This vector must characterize the fault signature and consequently the state of the machine. It is created by the magnitudes

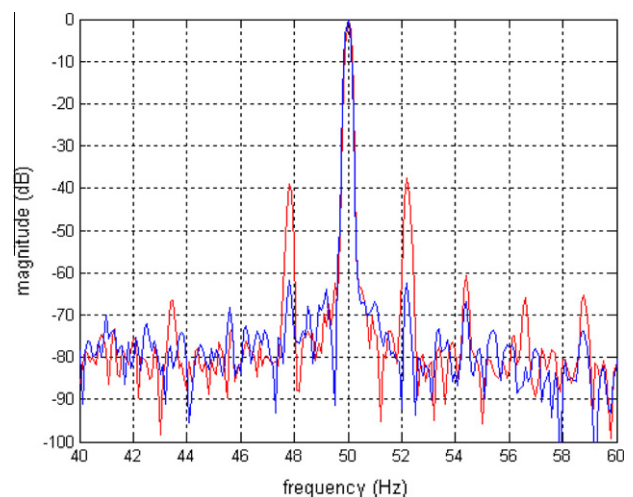


Fig. 11. MCSA spectrum of the loaded machine with broken rotor bar.

Table 4

Different frequency component (in hertz) related to the outer raceway bearing fault.

kf	100	200	300	400	500	600
$ Kf - 2f_d $	73.5	26.5	126.5	226.5	326.5	426.5
$Kf + 2f_d$	273.5	373.5	473.5	573.5	673.5	773.5

of the HPCSV spectral components relative to the studied faults. The vector is expressed as:

$$V = \begin{bmatrix} mag(3f + 2fs) \\ mag(3f - 2fs) \\ mag(9f + 2fs) \\ mag(9f - 2fs) \\ mag(2f) \\ mag(4f) \\ mag(f + 3f_r) \\ mag(f - 3f_r) \\ mag(2f + 3f_r) \\ mag(2f - 3f_r) \\ mag(2f + 2(0.4zf_r)) \\ mag(|2f - 2(0.4zf_r)|) \\ mag(4f + 2(0.4zf_r)) \\ mag(|4f - 2(0.4zf_r)|) \end{bmatrix} \quad (31)$$

The first stage in the recognition process is to create a database. It can be accomplished by analyzing the magnitudes of the HPCSV spectral components for the classes which represent the states of the induction machine. Here, there are five possibilities examined as following:

1. Machine operating without defect and supplied by a balanced voltage.
2. Machine operating without defect and supplied by an unbalanced voltage.
3. Machine operating with broken rotor bar.
4. Machine operating with an air-gap eccentricity fault.
5. Machine operating with an outer raceway bearing fault.

All these situations have been tested under the load rates 0%, 20%, 40%, 60%, 80% and 100% of the rated load. The data is divided into two data sets: the training data set (90 samples) and the testing data set (60 samples).

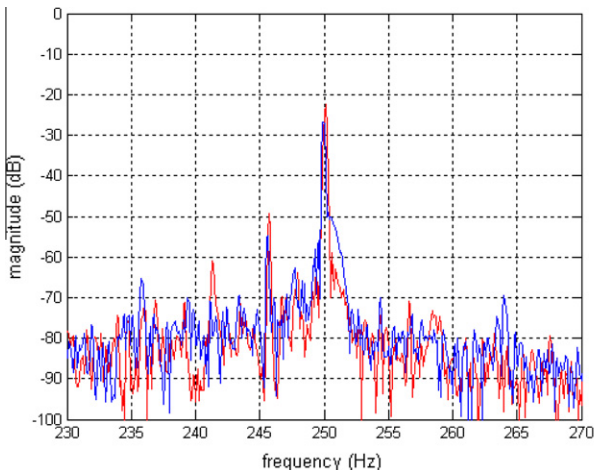


Fig. 12. MCSA Spectrums at full load in the case of broken rotor bar around 250 Hz and 350 Hz.

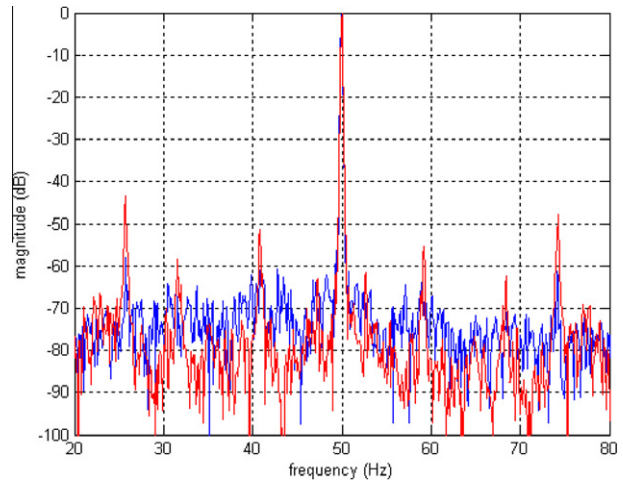


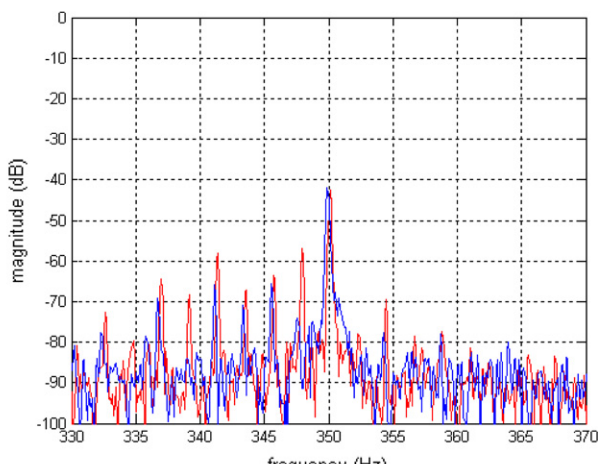
Fig. 13. MCSA spectrum of the loaded machine with air-gap eccentricity fault.

Table 5

Codification output of SVM.

	SVM1	SVM2	SVM3	SVM4
Normal condition	+1			
Broken rotor bar	-1	+1	-1	
Unbalanced voltage	-1	+1	+1	
Air-gap eccentricity fault	-1	-1		-1
Outer raceway bearing fault	-1	-1		+1

As shown in Fig. 16, the diagnostic model includes four SVM classifiers which are used to identify the five states: normal state and the four faults (broken rotor bar, unbalanced voltage, air-gap eccentricity, and outer raceway bearing fault). With all the training samples of the states, SVM1 is trained to separate the normal state from the fault state. When input of SVM1 is a sample representing the normal state, output of SVM1 is set to +1; otherwise -1. With the samples of single fault, SVM2 is trained to separate the mechanical fault from the electrical fault. When the input of SVM2 is a sample representing electrical fault, the output of SVM2 is set to +1; otherwise -1. With the samples of electrical fault, SVM3 is trained to separate the broken rotor bar from the unbalanced voltage. When the input of SVM3 is a sample representing the unbalanced voltage, the output of SVM3 is set to +1;



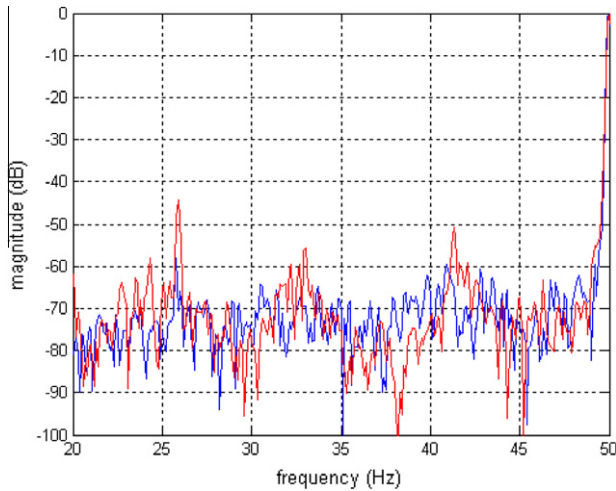


Fig. 14. MCSA spectrum of the loaded machine with outer raceway defect.

Table 6
The SVM classification performance.

SVM kernel function	False alarm rate (%)	Non-detection rate (%)
Polynomial	3.33% (2/60)	8.33% (5/60)
Gaussian	0%	5% (3/60)

otherwise -1 . With the samples of mechanical fault, SVM4 is trained to separate the air-gap eccentricity fault from the outer raceway bearing fault. When the input of SVM4 is a sample representing the outer raceway bearing fault, the output of SVM4 is set to $+1$; otherwise -1 .

All the four SVMs adopt polynomial and Gaussian as their kernel function. In SVM, the parameters σ and C of SVM model are optimized by the cross validation method. The adjusted parameters with maximal classification accuracy are selected as the most appropriate parameters. Then, the optimal parameters are utilized to train the SVM model. So the output codification is presented in Table 5.

The training procedure and choice of SVM parameters for training is very important for classification. Fig. 17 presents the process of optimizing the SVM parameters with the cross validation method. The false alarm rate and the non-detection rate of diagnostic systems for different membership functions are illustrated in Table 6. From Table 6, we note that the Gaussian kernel function shows highly accurate classification of fault diagnosis procedure. A classification rate of the fault diagnosis is 95%.

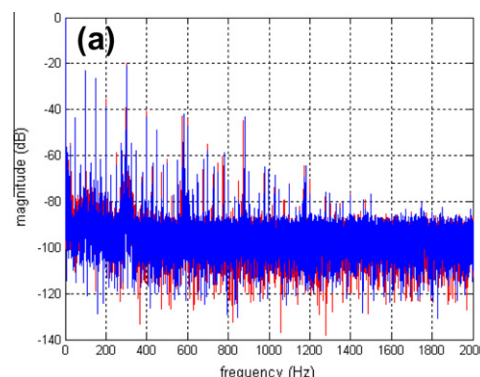


Fig. 15. Spectrums at full load in the range [0, 2000 Hz]: (a) HMCSV, (b) HPCSV.

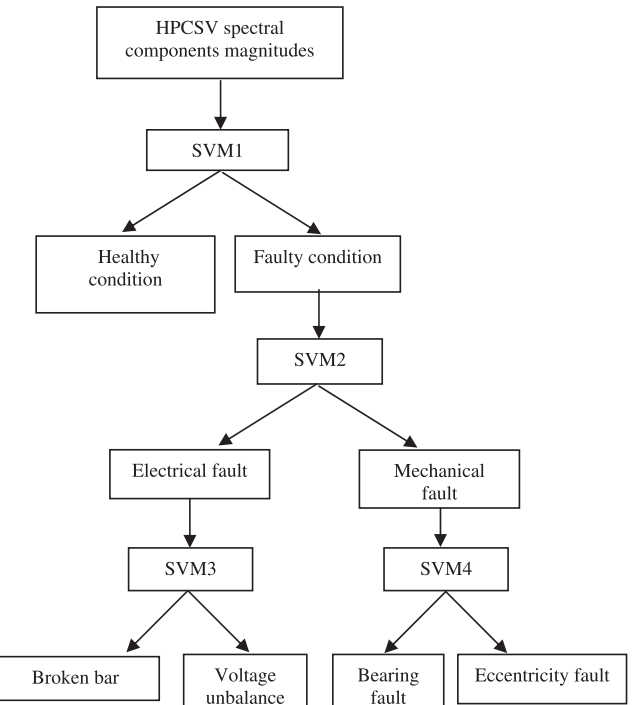


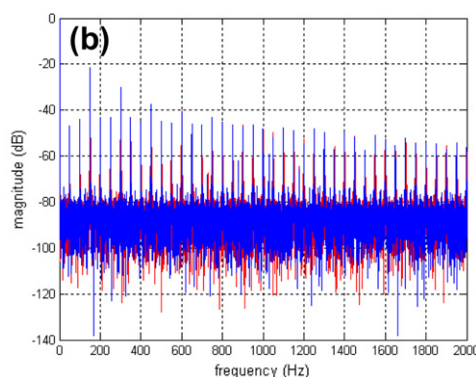
Fig. 16. Induction motor fault diagnostic model based on SVM classifiers.

5. Conclusions

An original fault signature based on an improved combination of Hilbert and Park transforms has been proposed. Starting from this combination, two fault signatures have been realized: Hilbert modulus current space vector (HMCSV) and Hilbert phase current space vector (HPCSV). These two signatures are subsequently analyzed using the classical fast Fourier transform (FFT). The effects of HMSCV and HPCSV spectrums are described and the related frequencies determined. A fault sensitivity comparative study of diagnosis media, related to broken rotor bars, supply voltage asymmetry, air-gap eccentricity fault and outer raceway ball bearing defect has been presented for a three-phase squirrel-cage induction machine.

Concerning the rotor fault and air-gap eccentricity conditions, it has been observed that for the tested induction machine, the related frequencies are more excited in the HPCSV than in the HMSCV.

Concerning the operating condition with voltage asymmetry, and outer raceway ball bearing defect the obtained results show



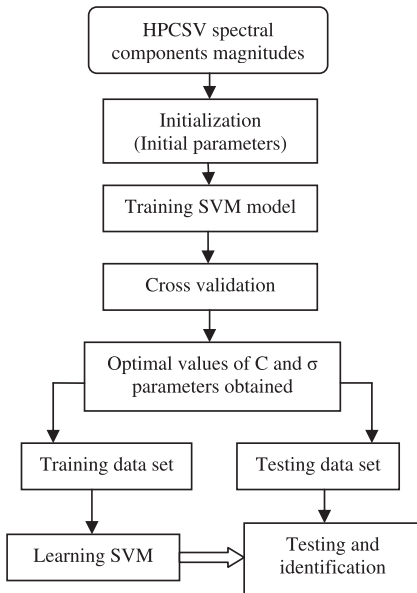


Fig. 17. Proposed method implementation basic steps.

a good performance for both HPCSV and HMCSV. For all the studied faults the HPCSV spectrum is richer in harmonics than the HMCSV spectrum. This study shows that for the detection of internal and external induction machine faults, HPCSV can be efficiently used for this purpose. The proposed fault signature shows its effectiveness and its robustness in both electrical and mechanical fault detection. In order to obtain a more robust diagnosis, it is proposed a support vector machine (SVM) suitable to online identification of induction machine faults: broken rotor bar, unbalanced voltage, air-gap eccentricity fault and outer raceway bearing defect. The input patterns to train the SVM are obtained using experimental data related to healthy and faulty machines under several load rates. The inputs of the SVM are very important for successful fault detection. In this work, we extract only the HPCSV spectral components magnitudes relative to the studied faults.

References

- [1] Chow M-Y. Guest editorial special section on motor fault detection and diagnosis. *IEEE Trans Ind Electron* 2000;47(5):982–3.
- [2] Sharifi Rasool, Ebrahimi Mohammad. Detection of stator winding faults in induction motors using three-phase current monitoring. *ISA Trans* 2011;50:14–20.
- [3] Tavakoli Bina M, Kashefi A. Three-phase unbalance of distribution systems: complementary analysis and experimental case study. *Int J Electr Power Energy Syst* 2011;33(4):817–26.
- [4] Chattopadhyay Surajit, Karmakar Subrata, Mitra Madhuchhanda, Sengupta Samarjit. Symmetrical components and current concordia based assessment of single phasing of an induction motor by feature pattern extraction method and radar analysis. *Int J Electr Power Energy Syst* 2012;37:43–9.
- [5] Mehrjou Mohammad Rezazadeh, Mariun Norman, Marhaban Mohammad Hamiruce, Misron Norhisam. Rotor fault condition monitoring techniques for squirrel-cage induction machine – a review. *Mech Syst Signal Process* 2011;25:2827–48.
- [6] Rajalakshmi Samaga BL, Vittal KP. Comprehensive study of mixed eccentricity fault diagnosis in induction motors using signature analysis. *Int J Electr Power Energy Syst* 2012;35:180–5.
- [7] Zarei Jafar. Induction motors bearing fault detection using pattern recognition techniques. *Expert Syst Appl* 2012;39:68–73.
- [8] Blödt Martin, Granjon Pierre, Raison Bertrand, Rostaing Gilles. Models for bearing damage detection in induction motors using stator current monitoring. *IEEE Trans Ind Electron* 2008;55(4):1813–22.
- [9] Jimenez Guillermo A, Munoz Alfredo O, Duarte-Mermoud Manuel A. Fault detection in induction motors using Hilbert and Wavelet transforms. *Electr Eng* 2007;89:205–20.
- [10] Aydin Ilhan, Karakose Mehmet, Akin Erhan. A new method for early fault detection and diagnosis of broken rotor bars. *Energy Convers Manage* 2011;52:1790–9.
- [11] Bacha K, Gossa M, Capolino GA. Comparative investigation of diagnosis media of stator voltage unbalance and rotor broken bars in induction motor. In: Proceeding of the 32nd annual conference on industrial, electronics IECON'2006; 6–10 November, 2006.
- [12] Zarei Jafar, Poshtan Javad. An advanced Park's vectors approach for bearing fault detection. *Tribol Int* 2009;42:213–9.
- [13] Cruz SMA, Marques Cardoso AJ. Stator winding fault diagnosis in three-phase synchronous and asynchronous motors, by the extended Park's vector approach. *IEEE Trans Ind Appl* 2001;37(5):1227–33.
- [14] Henao H, Demian C, Capolino GA. A frequency-domain detection of stator winding faults in induction machines using an external flux sensor. *IEEE Trans Ind Appl* 2003;39(5):1272–9.
- [15] Bedekar Prashant P, Bhide Sudhir R, Kale Vijay S. Fault section estimation in power system using Hebb's rule and continuous genetic algorithm. *Int J Electr Power Energy Syst* 2011;33(3):457–65.
- [16] Zhang Ya-Gang, Wang Zeng-Ping, Zhang Jin-Fang, Jing Ma. Fault localization in electrical power systems: a pattern recognition approach. *Int J Electr Power Energy Syst* 2011;33(3):791–8.
- [17] Bacha K, Souahlia S, Gossa M. Power transformer fault diagnosis based on dissolved gas analysis by support vector machine. *Electr Power Syst Res* 2012;83:73–9.
- [18] Bacha K, Henao H, Gossa M, Capolino G-A. Induction machine fault detection using stray flux EMF measurement and neural network-based decision. *Electr Power Syst Res* 2008;78:1247–55.